Functionalization of Biomass Carbonaceous Aerogels: Selective Preparation of MnO$_2$@CA Composites for Supercapacitors

Yumei Ren,[†] Qun Xu,*[,†] Jianmin Zhang,[†] Hongxia Yang,[†] Bo Wang,[†] Daoyuan Yang,[†] Junhua Hu,[†] and Zhimin Liu*[,‡]

[†]College of Materials Science and Engineering, Zhengzhou University, Zhengzhou 450052, People's Republic of China
[‡]Institute of Chemistry, Chinese Academy of Sciences, Beijing 100080, People's Republic of China

Ⓢ Supporting Information

ABSTRACT: Functionalized porous carbon materials with hierarchical structure and developed porosity coming from natural and renewable biomass have been attracting tremendous attention recently. In this work, we present a facile and scalable method to synthesize MnO$_2$ loaded carbonaceous aerogel (MnO$_2$@CA) composites via the hydrothermal carbonaceous (HTC) process. We employ two reaction systems of the mixed metal ion precursors to study the optimal selective adsorption and further reaction of MnO$_2$ precursor on CA. Our experimental results show that the system containing KMnO$_4$ and Na$_2$S$_2$O$_3$·5H$_2$O exhibits better electrochemical properties compared with the reaction system of MnSO$_4$·H$_2$O and (NH$_4$)$_2$S$_2$O$_8$. For the former, the obtained MnO$_2$@CA displays the specific capacitance of 123.5 F·g^{-1}. The enhanced supercapacitance of MnO$_2$@CA nanocomposites could be ascribed to both electrochemical contributions of the loaded MnO$_2$ nanoparticles and the porous structure of three-dimensional carbonaceous aerogels. This study not only indicates that it is vital for the reaction systems to match with porous carbonaceous materials, but also offers a new fabrication strategy to prepare lightweight and high-performance materials that can be used in energy storage devices.

KEYWORDS: carbonaceous materials, aerogel, MnO$_2$, supercapacitors
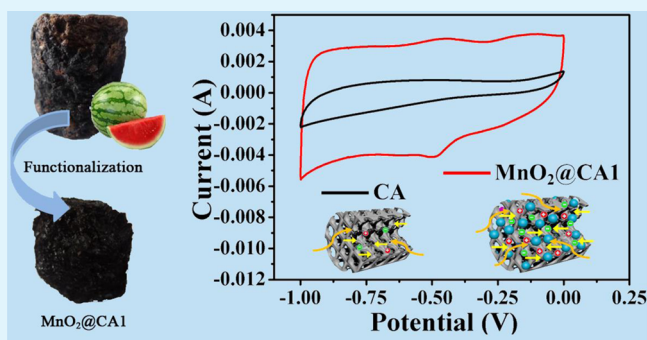
INTRODUCTION

In recent years, concentrated efforts have been made to design and develop new advanced materials for energy storage, due to the demand of high energy and high power density. Supercapacitors, one of the most promising electrochemical energy storage systems, have received increasing attention, as they possess high power capability, excellent cycle stability and reversibility, etc.[1−3] Currently, one of the great challenges being faced is to provide low-cost and environmentally benign high-power energy resources.

Carbon-based materials have received the most attention for their remarkable and unusual physicochemical properties, motivated by their potential importance in separation science, heterogeneous catalyst supports, and water purification filters, and as well as the developing areas of energy generation and storage.[4,5] To date, the utilization of various carbonaceous materials, such as activated carbons,[6] carbon fibers,[7] CNTs,[8,9] graphene,[10,11] carbon spheres, and carbon aerogels,[12−18] has been investigated extensively as the electrode materials for supercapacitors. Although they have high power density and long cycle life, the relatively low specific capacitance greatly limits their application in commercialized supercapacitor devices.[19,20] Compared with the carbon-based electrode

materials, typical active pseudocapacitive materials, including transition metal oxides such as RuO$_2$, Fe$_3$O$_4$, NiO, and MnO$_2$, and conducting redox polymers such as polyanilines, polypyrroles, and polythiophenes, have been studied generally as active electrode materials for supercapacitors featured with high energy density and large charge transfer reaction.[21−27] Of these pseudocapacitive electrode materials, MnO$_2$ is considered to be one of the most promising alternative electrode materials for a high-performance supercapacitor, benefiting from its low-cost, environmental benignity, and natural abundance.[28−31] However, it suffers from poor electrical conductivity, which largely prevents its widespread practical application.[30,31] Recent studies have shown that the combination of MnO$_2$ and carbonaceous material can successfully improve the specific capacitance of supercapacitor devices, as it enables the resultant compounds with the synergy of electric double layer capacitance and pseudocapacitance.[28,30−34]

Biomass, such as carbohydrates, crude plants, and others, has been used as a promising starting material for the synthesis of
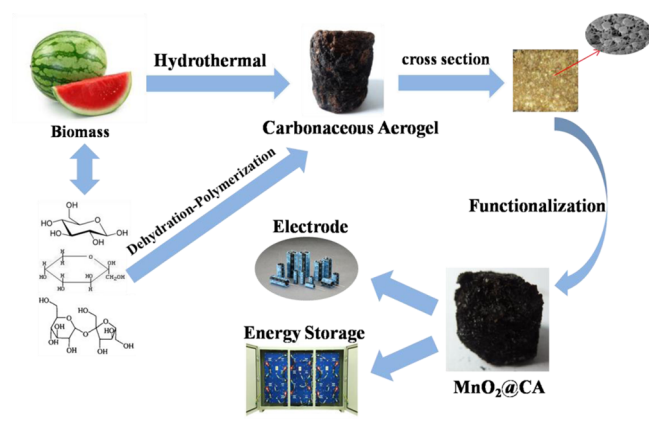
functional carbonaceous materials.[35−37] Until now, many synthetic methods have been established to prepare carbon materials, while most of them require harsh and rather expensive processing conditions.[38,39] A hydrothermal carbonization (HTC) process is a promising route to produce functional carbonaceous materials, considering its relatively mild temperatures and high carbon efficiency.[19,34,40−43] Besides, the obtained biomass-derived carbonaceous materials not only have hierarchical porous nanoarchitecture, but also contain abundant functional groups that can greatly improve their hydrophilicity and chemical reactivity.[37]

Herein, we apply a simple and facile hydrothermal approach to synthesize MnO_2@CA composites as electrode materials for supercapacitors. The experimental sketch of our idea has been illustrated in Scheme 1. In this work, we choose watermelon as

Scheme 1. Illustration of the Synthetic Strategy and Further Application for the Functional Carbonaceous Materials That Come from Watermelon

the research object. After hydrothermal carbonization and freeze-drying process, porous carbonaceous aerogels can be obtained. In order to obtain the high-performance electrode materials, further functionalization on the carbonaceous aerogels with precursors of MnO_2 are adopted. Two reaction systems, (1) $KMnO_4$+$Na_2S_2O_3$·$5H_2O$ system and (2) $MnSO_4$·H_2O+$(NH_4)_2S_2O_8$ system, are employed to help obtaining the MnO_2@CA. It is anticipated that such method can be explored successfully to synthesize functionalized carbonaceous materials by using the sustainable biomass materials as the carbon precursors, which is environmentally benign and reproducible.

■ EXPERIMENTAL SECTION

All the chemicals were analytic grade reagents used without further purification. Potassium permanganate ($KMnO_4$, purity: ≥ 99%), Sodium thiosulfate pentahydrate (NaS_2O_3·$5H_2O$, purity: ≥99%), Manganese sulfate monohydrate ($MnSO_4$·H_2O, purity: ≥99%), Ammonium persulfate (($NH_4)_2S_2O_8$, purity: ≥98%), Potassium hydroxide (KOH, purity: ≥85%), dehydrated alcohol (CH_3CH_2OH, purity: ≥99.7%), deionized water, and watermelon as the carbon resource.

Sample Preparation. The carbonaceous hydrogel (CG) was prepared by a simple hydrothermal process directly from the soft tissue biomass of watermelon. Watermelon was first cut into the appropriate volume and then put it into the corresponding Teflon-lined stainless steel autoclave. After that, the autoclave was put into an oven and heated at 180 °C for 12 h. The obtained carbonaceous hydrogel monolith was washed by deionized water and dehydrated alcohol (the volume ratio is 1:1) several times to remove the soluble impurities.

Then corresponding carbonaceous aerogel (CA) was obtained by freeze-drying at −42 °C for 2 h, followed by drying at 60 °C for 12 h.

MnO_2@CA composite materials were also synthesized under hydrothermal conditions. For the system of $KMnO_4$ and $Na_2S_2O_3$·$5H_2O$, in a typical procedure, the mole ratio of CA and potassium permanganate is 20:1. The mole ratio of sodium thiosulfate pentahydrate and potassium permanganate is 1:2. While for the system of $MnSO_4$·H_2O and ($NH_4)_2S_2O_8$, the mole ratio of CA and manganese sulfate monohydrate is 20:1, the mole ratio of ammonium persulfate and manganese sulfate monohydrate is 1:2. Then they were dissolved in deionized water to form the precursor solution. To prepare the MnO_2@CA composite material, the carbonaceous aerogel was first cut into small sizes by a sharp knife to wipe off its hard surface. Then, the obtained piece of CA was fully immersed in the precursor solution, which was then transferred into a Teflon-lined stainless steel autoclave (the ratio volume of solution/volume of autoclave is around 0.6). The autoclave was sealed and maintained at 120 °C for 12 h. Then the autoclave was allowed to cool to room temperature naturally. The obtained samples were filtered, washed several times with deionized water and dehydrated alcohol to remove impurities and excess ions, and then dried in air at 60 °C for 24 h. The as-prepared samples were calcined in N_2 atmosphere at 350 °C for 2 h.

Characterizations. The structure of the materials was characterized by Field-emission scanning electron microscope (FE-SEM, JSM7500F) and transmission electron microscopy (TEM) (JEM-2100). X-ray diffraction (XRD) patterns of samples were measured on a Y-2000 X-ray Diffractometer with copper Kα radiation (λ = 1.5406 Å) operating at 40 kV and 40 mA. The Raman measurements were carried out on a Renishaw Microscope System RM2000 with a 50 mWAr$^+$ laser at 514.5 nm. Fourier transform infrared spectra (FTIR) were recorded on a TENSOR 27 FTIR spectrometer (Bruker) in the absorption mode with resolution of 2 cm^{-1} to determine the surface functional groups of the carbonaceous gels. The specific surface areas and pore size distributions of the electrode materials were calculated by Brunauer−Emmett−Teller (BET), N_2 adsorption isotherms at 77 K using a Micromeritics ASAP 2020 system. Then the samples were degassed at 300 °C for 10 h. Thermogravimetric analysis (TGA) was carried out in a SMP/PF7548/MET/600W thermogravimetric analyzer from 50 to 700 °C with a heating rate of 20 °C min^{-1} in air flow.

Electrochemical Measurements. A three-electrode configuration was used to measure the electrochemical behaviors of the electrode materials. Cyclic voltammetry (CV), galvanostatic charge/discharge, and electrochemical impedance spectroscopy (EIS) experiments were performed on a CHI 660D electrochemical workstation at room temperature. The working electrode was prepared by mixing 80 wt % MnO_2@CA composite material, 10 wt % polytetrafluoroethylene (PTFE) used as a binder, and 10 wt % carbon black. The mixture was spread and pressed onto nickel foam (1 × 1 cm^2). After the electrode materials were loaded, the working electrode was pressed and dried in vacuum at 80 °C for 12 h. The auxiliary and reference electrode were Pt foil and Ag/AgCl, respectively. The electrolyte used in all of the measurements was a 6 M KOH solution. The potential range for CV tests was −1.0 to 0 V, and the scan rate was 5, 10, 20, 50, and 100 mV·s^{-1}. Galvanostatic charge/discharge measurements were done from −1.0 to 0 V with different current densities at 0.5, 1, 2, 4, 6, and 10.0 A·g^{-1}. Electrochemical impedance spectroscopy (EIS) measurements were carried out in a frequency range of 0.01 Hz to 100 kHz with AC amplitude of 5 mV.

■ RESULTS AND DISCUSSION

The monolithic carbonaceous hydrogel (CG) (Figure 1a) was produced via a simple hydrothermal carbonization (HTC) process from the soft tissue of watermelon. During the initial stages of the HTC process, hydroxymethyl furfural (HMF) and furfural are formed, which are the dehydration products of the carbohydrate.[38,44] Next, a series of polymerization−polycondensation reactions take place and enable the formation of polyfuranic structure. Then the polyfuranic chains react further
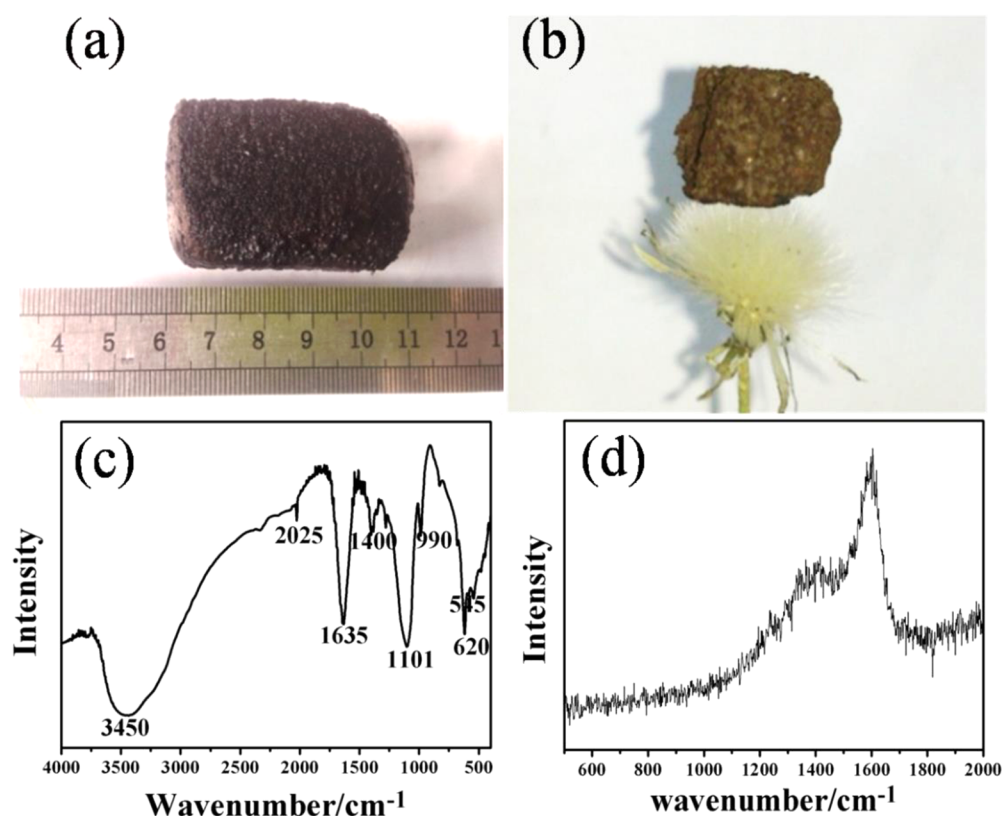
Figure 1. (a) Photograph of the carbonaceous hydrogel monolith; (b) a carbonaceous aerogel standing on a dandelion; (c) FT-IR spectra of carbonaceous aerogel; and (d) Raman spectra of carbonaceous aerogel.

to obtain the aromatic networks.[24,38] Through further freeze-drying, the 3D porous carbonaceous aerogel (CA) (Figure 1b) can be obtained, and the color of it turned from black to brown. Figure 1b also shows that the CA is lightweight for it can stand on a dandelion. The mass density of the CA was measured to be about 21.7 mg·cm^{-3}. In addition, the volumes of the CA monolith can be tuned by cutting the fresh watermelon into monoliths with different sizes (Supporting Information (SI) Figure S1,) and using the corresponding volumetric autoclaves.

Fourier transform infrared (FT-IR) spectroscopy (Figure 1c) was used to identify the surface functional groups of the resulting CA. The broad and strong band at ca. 3450 cm^{-1} is attributed to the O—H stretching vibrations. The observed bands at ca. 1635 cm^{-1} are attributed to the C=O or C=C stretching vibrations, indicating the existence of furanic or aromatic groups.[34,37,42] The bands at about 1400 cm^{-1} can be attributed to C—H in-plane bending vibration. The bands at 1101 cm^{-1} is ascribed to the C—O—C stretching vibration or C—C framework vibration.[42] The bands at 990 and 620 cm^{-1} are ascribed to deformation vibration of vinyl C—H and C—H plane bending vibration, respectively.[39] The FT-IR result indicates that the surfaces of the obtained CA are rich in hydroxyl, carbonyl, carboxyl, and aromatic groups. Such surface groups provide the possibilities for their further functionalization, which make the materials more hydrophilic and highly dispersible in water.[37] Raman spectra of CA shows that the broad and strong bands at about 1580 and 1358 cm^{-1} can be attributed to the in-plane bond-stretching motion of the pairs of C-sp^2 atoms and the disorder-induced mode associate with structure defects and imperfections, respectively (Figure 1d).[45−47] Therefore, the intensity ratio of D and G bands (I_D/I_G) may reflect the extent of disordered structure. The

calculated I_D/I_G ratio for CA is 0.3097, suggesting that it was highly graphitized.

Scanning electron microscopy (SEM) and transmission electron microscopy (TEM) were used to observe the internal morphology and structure of CA. SEM and TEM images reveal that the obtained CA consists of both global catenulate (Figure 2a,c) and carbon nanofibers network cross-linked with carbon nanospheres (Figure 2b,d), which constitute the 3D porous structure.[43] The size of the final nanospheres and nanofibers of the CA is highly dependent on the time and temperature of hydrothermal carbonization.[40] In addition, substantial oxygen-containing functional groups on the surface of carbonaceous
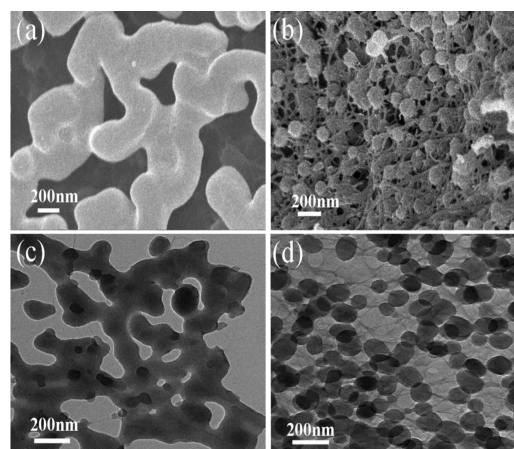

Figure 2. SEM images (a,b) and TEM images (c,d) of carbonaceous aerogel.

gels make it easily processable, which enable them to be a good scaffold for the synthesis of 3D composite materials.[33] Next, we try to develop a facile hydrothermal process for growing MnO_2 nanoparticles on carbonaceous aerogels from the solution of mixed metal ion precursors.[48−51] Two reaction systems were chosen to study the optimal selective adsorption and reaction on CA, i.e., the first system of $KMnO_4$ and $Na_2S_2O_3·5H_2O$, and the second system of $MnSO_4·H_2O$ and $(NH_4)_2S_2O_8$. Further, the conductive $MnO_2@CA$ composites are fabricated by calcinations.[34] The obtained nanocomposites are labeled $MnO_2@CA1$ and $MnO_2@CA2$, respectively. The detail illustration of experimental process of the $MnO_2@CA1$ composite is presented as SI Figure S2.

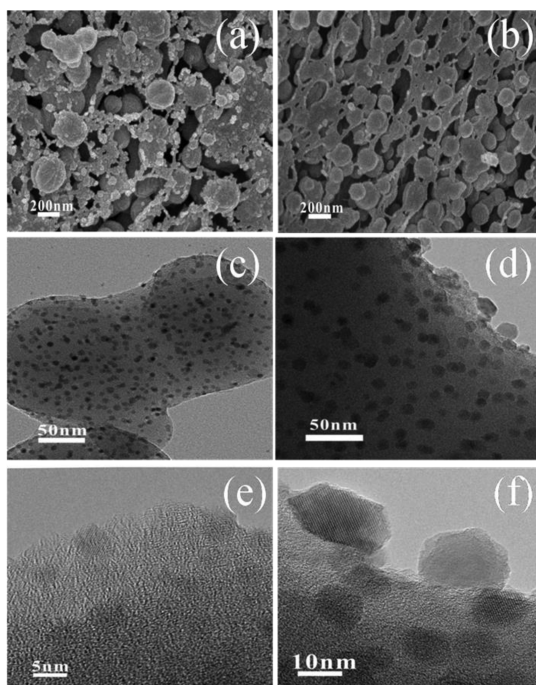Figure 3a,b shows the cross section of $MnO_2@CA1$ and $MnO_2@CA2$. Their SEM images indicate that they both inherit

Figure 3. SEM images of the cross section of $MnO_2@CA1$ (a) and $MnO_2@CA2$ (b), TEM images of $MnO_2@CA1$, $MnO_2@CA2$ at low magnification (c,d) and high magnification (e,f).

the monolithic architecture of the original CA even after the calcination process. TEM images (Figure 3c,d) reveal the excellent dispersion of MnO_2 nanoparticles inside the 3D carbon networks. From the magnified TEM images, as shown in Figure 3e,f, it can be observed that the small MnO_2 nanoparticles with an average size of about 5 nm incorporated in $MnO_2@CA1$, while larger MnO_2 nanoparticles with average size of about 15 nm are incorporated in $MnO_2@CA2$. There are more TEM images of $MnO_2@CA1$ and $MnO_2@CA2$ that can be seen in SI Figures S3 and S4. From the characterization images of TEM, it can be observed that for $MnO_2@CA1$, most MnO_2 nanoparticles are inserted into CA1. While for $MnO_2@$ CA2, apparently more MnO_2 nanoparticles grew on the surface of CA2. The various size and dispersion of MnO_2 on carbon aerogels may have a profound effect on their further functionality. N_2 sorption isotherms analysis was conducted to determine the porosity of CA. The nitrogen adsorption and desorption isotherms and the pore size distribution curve are provided in Figure 4. The experimental results indicate that the
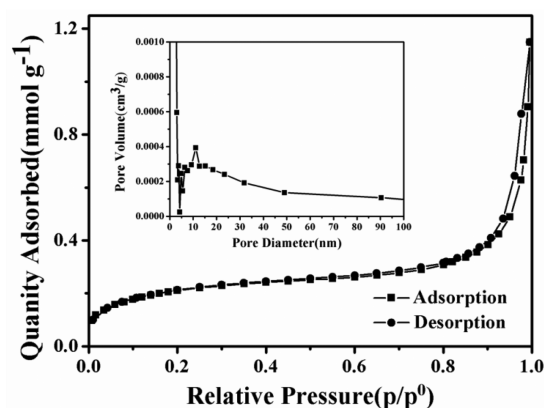

Figure 4. Nitrogen adsorption−desorption isotherm and its corresponding pore size distributions (inset) of the carbonaceous aerogel.

average pore diameter of CA was 5.4 nm and the most probable distribution of pore size was lower than 11 nm. Considering the average size of MnO_2 nanoparticles in $MnO_2@CA1$ are 5 nm, and that of MnO_2 in $MnO_2@CA2$ are 15 nm, therefore, it is deduced that for $MnO_2@CA1$, the smaller MnO_2 nanoparticles are inserted inside the carbonaceous aerogels, while for $MnO_2@CA2$, MnO_2 nanoparticles are on the surface of carbonaceous aerogels. And this phenomenon can be further confirmed in the following study of TGA.

X-ray diffraction (XRD) measurements are used to investigate the crystal structure of the resultant materials. As shown in Figure 5a, the existence of MnO_2 can be confirmed, and the comparatively weak peaks indicate that MnO_2 is in microcrystal structure. The weak diffraction peaks of MnO_2 mainly correspond to the (200), (310), (220), (400), (600), and (521), which are in good agreement with α-MnO_2.[52,53] Figure 5b shows the TGA of $MnO_2@CA1$, $MnO_2@CA2$, and CA, respectively. The experiment was performed from 50 to 700 °C with a ramp heating rate of 20 °C min^{-1} in air atmosphere.[45] The CA lost 98.67 wt % at ca. 545 °C, while the mass losses of $MnO_2@CA1$ and $MnO_2@CA2$ were 79.48% and 97.12%, respectively. From the residue, it can be calculated that the amount of MnO_2 in $MnO_2@CA1$ is about 12.4 times higher than that in $MnO_2@CA2$. In the initial stage, the small mass loss of these samples is due to the removal of adsorbed water and dehydration of them.[47,54,55] The distinct mass loss in the range of 260−430 °C ($MnO_2@CA1$) and 290−600 °C ($MnO_2@CA2$) observed in the TGA data is related to the removal of carbon from the composites as well as the phase transition of MnO_2.[45,54−56] Figure 5c,d shows the TGA-DTA curves of $MnO_2@CA1$ and $MnO_2@CA2$. It can be clearly seen that $MnO_2@CA1$ has only one exothermic peak at ca. 350 °C, which corresponds to the phase transition from α-MnO_2 to Mn_3O_4.[54,57] While $MnO_2@CA2$ has two exothermic peaks at ca. 350 and 500 °C, which corresponds to the phase transition from α-MnO_2 to Mn_3O_4 and Mn_3O_4 to Mn_2O_3, respectively.[56,57] This may be due to the fact that the MnO_2 nanoparticles of $MnO_2@CA1$ embedded in the 3D carbon networks and the substrate of carbon aerogel can effectively protect the MnO_2 nanoparticles from further transforming into other oxide phases at higher temperatures. Furthermore, TGA thermograms of MnO_2 in $MnO_2@CA1$ and $MnO_2@CA2$ are employed to explain the calcination temperature we used (SI Figure S5). It can be seen that the curves of reach a stable level
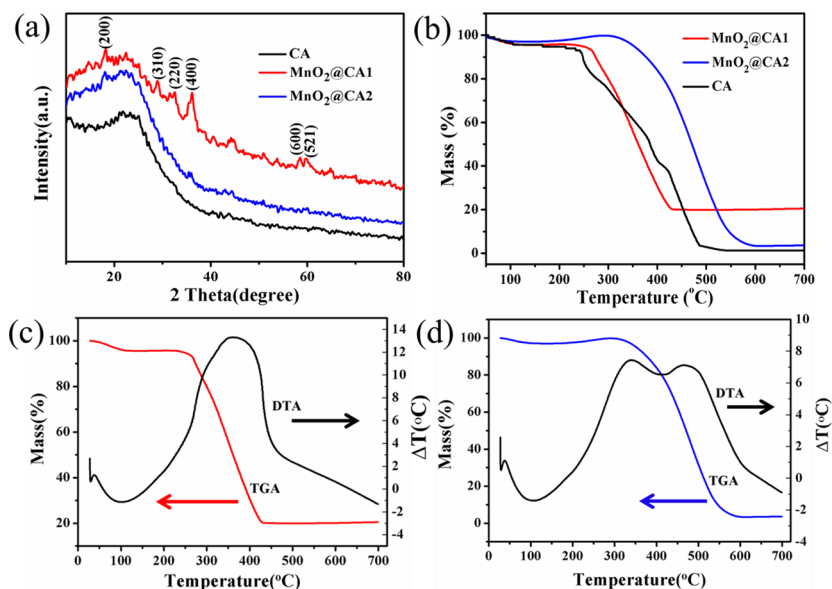
Figure 5. XRD patterns (a) and thermogravimetric analysis (TGA) curves (b) of MnO_2@CA1, MnO_2@CA2, and CA. TGA and DTA curves of MnO_2@CA1 (c) and MnO_2@CA2 (d).

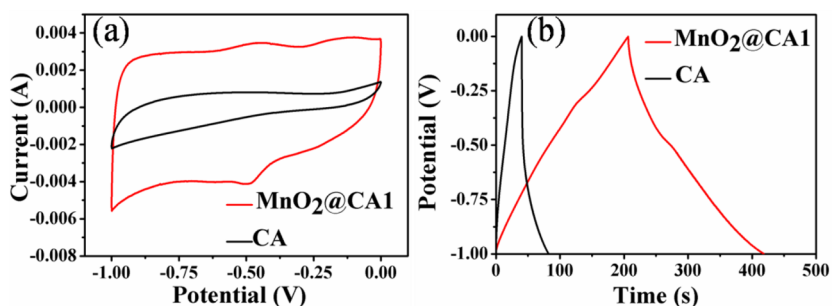**Figure 6.** (a) Cyclic voltammetry (CV) curves of CA and MnO_2@CA1 electrode in 6 M KOH aqueous electrolyte, scan rates: 5 mV·s^{-1}. (b) Charge/discharge curves of the CA and MnO_2@CA1 electrode, constant current densities: 0.5 A·g^{-1}.
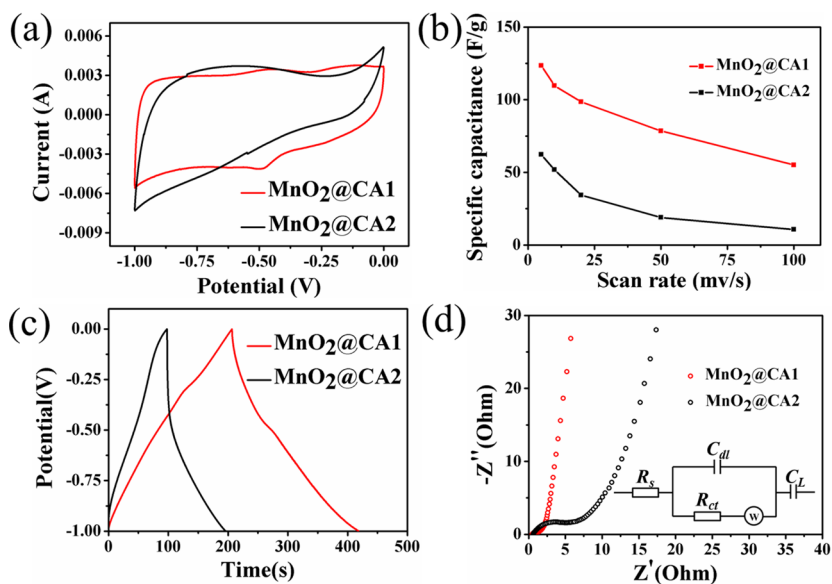

Figure 7. (a) CV curves of MnO_2@CA1 and MnO_2@CA2 electrode materials in 6 M KOH aqueous electrolyte, scan rates: 5 mV·s^{-1}. (b) Calculated specific capacitances from the CV curves of MnO_2@CA1 and MnO_2@CA2 electrode materials at different scan rates. (c) Charge/discharge curves of MnO_2@CA1 and MnO_2@CA2 electrode, constant current densities: 0.5 A·g^{-1}. (d) Nyquist plots of MnO_2@CA1 and MnO_2@CA2 electrode materials. The inset is the equivalent circuit.

in the range of ca. 350–530 °C, which suggests that the lattice of MnO_2 is steady. So we chose 350 °C as the calcination temperature.

In order to get more information on the properties of MnO_2@CA composite, we made the contrast experimental studies about the electrochemical performance of MnO_2@CA and CA. The CA was also calcined in N_2 atmosphere at 350 °C for 2 h. The electrochemical performances of the obtained MnO_2@CA nanocomposite electrode materials were conducted to investigate the contribution of MnO_2 by cyclic voltammetry (CV) and galvanostatic charge/discharge within the potential window between −1.0 and 0 V in 6 M KOH aqueous solution. Figure 6a shows the CV date of CA and MnO_2@CA1 electrode with a scan rates of 5 mV·s^{-1}. It can be clearly seen that for MnO_2@CA1, it exhibits nearly rectangular shapes that indicate ideal capacitive behavior, while CA has low capacitances. The galvanostatic charge/discharge analytic results of CA and MnO_2@CA1 electrodes are shown in Figure 6b. The CA has a shorter discharging period, indicating the lower capacitance, which is consistent with the CV date. Compared with CA, the discharging time of MnO_2@CA1 is apparently longer than CA, and it is suggested that MnO_2@CA1 possesses good electrochemical performances. So these experimental results indicate that the enhanced specific capacitance is mainly due to the synergistic effect of CA and MnO_2 nanoparticles. For the nanocomposite of MnO_2@CA1, CA can form a porous three-dimensional conducting network for fast electron transfer and act as the support for the growth of MnO_2 as well.[58] At the same time, MnO_2 attached on the CA can effectively reduce the diffusion length of the electrolyte.[46]

From the study above, it can be suggested that MnO_2-modified CA has an apparent improved electrochemical performance compared to pure CA. Next we need to know which reaction system is the optimal one to achieve the excellent electrochemical properties when they are used as the electrode materials. In the following, we investigated the electrochemical properties of MnO_2@CA1 and MnO_2@CA2 (Figure 7). As shown in Figure 7a, the CV curve of MnO_2@CA1 at a scan rate of 5 mV·s^{-1} has a more rectangular shape and larger loop area than that of MnO_2@CA2, indicating that MnO_2@CA1 exhibited lower resistance and better capacitive behavior.[59] The specific capacitances of MnO_2@CA obtained from the CV curves can be quantitatively calculated by the equation $C = (\Delta S)/(2vmu)$, where C is the specific capacitance (F·g^{-1}), ΔS is the area of the CV curves, u is the potential window (V), v is the scan rate (mV·s^{-1}), and m is the mass of the sample used for the electrochemical test (g) excluding the binder and conductive carbon black. The MnO_2@CA1 electrode exhibits a relatively high specific capacitance achieved of 123.5 F·g^{-1} at 5 mV·s^{-1}. The value of specific capacitance of MnO_2@CA2 was 62.3 F·g^{-1} at the same scan rate. The CV curves of the two systems measured at potential sweep rates of 5–100 mV·s^{-1} are shown in SI Figure S6a,c, respectively. Figure 7b shows the calculated specific capacitances at different scan rates, in which the MnO_2@CA1 electrode shows the best capacitance performance in a wide scan rate range.

Figure 7c shows the galvanostatic charge/discharge results of MnO_2@CA1 and MnO_2@CA2 with a constant current density at 0.5 A·g^{-1}. The specific capacitance of the electrode material was calculated from the discharge curve according to $C = I \cdot \Delta t/(\Delta V \cdot m)$, where I is the discharge current (A), Δt is the discharge time (s), ΔV is the voltage change (V) excluding IR

drop in the discharge process, and m is the mass of the electrode material (g), excluding the binder and conductive carbon black. The presence of the IR drop at the beginning of discharge is usually associated with the equivalent series resistance (ESR) phenomenon.[60] The specific capacitance of MnO_2@CA1 from the discharge curve is calculated to be 106.4 F·g^{-1}, while MnO_2@CA2 shows lower specific capacitance of 49.3 F·g^{-1} at the same current density. The high capacitance of MnO_2@CA1 is mainly due to the high content of MnO_2, which can provide more pesudocapacitance contribution.[46,61,62] The galvanostatic charge/discharge behavior of the MnO_2@CA electrode was also tested at current densities from 0.5 to 10 A·g^{-1} (SI Figure S6b,d).

Electrochemical impedance spectroscopy (EIS) provides important information about the interfacial properties of electrodes, which was used to examine their conductive and diffusive behavior.[19,62,63] It was carried out in a frequency range from 0.01 Hz to 100 kHz (Figure 7d). The equivalent circuit fitting the Nyquist plots is shown in inset of Figure 7d. The semicircular part at higher frequencies corresponds to the charge transfer process at electrode/electrolyte interface, and its diameter is equivalent to the Faradaic charge transfer resistance (R_{ct}).[32,56] Solution resistance (R_s) is the intersection of the curve at real part Z' in the high frequency range. It is a combinational resistance of ionic resistance of electrolyte, intrinsic resistance of substrate, and contact resistance between electrode and current collector.[32,46] The slope of the curves at a low frequency is called Warburg impedance (W), which is induced by ion diffusion/transport from the electrolyte to the electrode surface.[46] Comparing the Nyquist plots of MnO_2@CA1 and MnO_2@CA2, we can clearly observe that a smaller diameter of semicircular at the high frequency region for MnO_2@CA1 than that of MnO_2@CA2, indicating that the higher conductivity achieved in the MnO_2@CA1 system. And the more vertical shape at lower frequencies for MnO_2@CA1 also indicates the better capacitive behavior of the electrode materials. Furthermore, consecutive galvanostatic charge/discharge cycling test of the MnO_2@CA1 electrode was measured in the range of −1–0 V at 1 A·g^{-1} in 6 M KOH aqueous solution (SI Figure S7). It can be seen that the MnO_2@CA1 electrode maintained over 60% of the initial specific capacitance after 1000 cycles.

The experimental results above indicate that the electrochemical performance of MnO_2@CA1 is apparently higher than that of MnO_2@CA2. The excellent electrochemical performance of the MnO_2@CA1 composite may be due to its unique architecture as illustrated in Figure 8. For MnO_2@CA1, from the characterization and analysis of SEM, TEM, BET, and TGA, it can be suggested that the smaller MnO_2
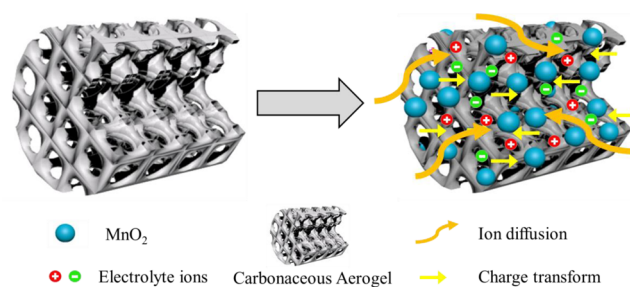

Figure 8. Schematic illustration for the electrochemical performance of MnO_2@CA1 composite.

nanoparticles are inserted inside the carbonaceous network, which not only increases the interfacial contact between MnO_2 and CA, but also enhances the effective interfacial area between MnO_2 and the electrolyte. In addition, the relatively high mass loading of active MnO_2 on CA can provide the pseudocapacitance, which can distinctly improve the specific capacitance. While for $MnO_2@CA2$, the larger MnO_2 nanoparticles cannot be inserted into the porous architecture of the carbon aerogel, so it does not facilitate the diffusion of the electrolyte. Therefore, a conclusion can be drawn from this study that different reaction systems utilized in the biomass substrate can be induced to various functionality. And it is important to choose the appropriate reaction system for the functionalization of biomass materials.

CONCLUSIONS

In summary, we have demonstrated a simple and cost-effective method to synthesize $MnO_2@CA$ composites from natural and renewable biomass. The experimental results indicate that the ideal electrochemical performance of electrode materials can be obtained from the synergistic effect of excellent hierarchical structure and active component. Two reaction systems were chosen and compared, confirming that the system of $KMnO_4$ and $Na_2S_2O_3\cdot5H_2O$ exhibits better electrochemical properties than the system of $MnSO_4\cdot H_2O$ and $(NH_4)_2S_2O_8$. The $KMnO_4$ system displays a specific capacitance as high as 123.5 $F\cdot g^{-1}$ at 5 $mV\cdot s^{-1}$. Furthermore, this hybrid material strategy opens up possibilities to combine the CA with other redox pseudocapacitive materials like polyaniline, polypyrrole, NiO, and Co_3O_4 by choosing appropriate precursors which can interact with the CA to enhance the energy density of supercapacitors.

ASSOCIATED CONTENT

Ⓢ Supporting Information

Photograph of the carbonaceous hydrogel monoliths with different volumes; illustrative fabrication process of the $MnO_2@CA$ composites using the system of $KMnO_4$ and $Na_2S_2O_3\cdot5H_2O$; TEM images of $MnO_2@CA1$ and $MnO_2@CA2$; Thermogravimetric analysis (TGA) curves of MnO_2; and CV and charge/discharge curves of $MnO_2@CA1$ and $MnO_2@CA2$ at the mole ratio of CA and $KMnO_4$ is 20:1. Cycling performance of $MnO_2@CA1$ electrode at a charge/discharge current density of 1 $A\cdot g^{-1}$ in 6 M KOH solution. This material is available free of charge via the Internet at http://pubs.acs.org.

AUTHOR INFORMATION

Corresponding Authors
*Fax: +86 371 67767827; E-mail: qunxu@zzu.edu.cn.
*Tel.: +86 371 67767827; E-mail: liuzm@iccas.ac.cn.

Notes
The authors declare no competing financial interest.

ACKNOWLEDGMENTS

REFERENCES

(1) Simon, P.; Gogotsi, Y. Materials for Electrochemical Capacitors. *Nat. Mater.* 2008, 7, 845−854.

(2) Merlet, C.; Rotenberg, B.; Madden, P. A.; Taberna, P. L.; Simon, P.; Gogotsi, Y.; Salanne, M. On the Molecular Origin of Supercapacitance in Nanoporous Carbon Electrodes. *Nat. Mater.* 2012, 11, 306−310.

(3) Chen, Zh.; Qin, Y. Ch.; Weng, D.; Xiao, Q. F.; et al. Design and Synthesis of Hierarchical Nanowire Composites for Electrochemical Energy Storage. *Adv. Funct. Mater.* 2009, 19, 3420−3426.

(4) Nardecchia, S.; Carriazo, D.; Ferrer, M. L.; Gutierrez, M. C.; Monte, F. Three Dimensional Macroporous Architectures and Aerogels Built of Carbon Nanotubes and/or Graphene: Synthesis and Applications. *Chem. Soc. Rev.* 2013, 42, 794−830.

(5) Huang, Y.; Liang, J. J.; Chen, Y. S. An Overview of the Applications of Graphene-Based Materials in Supercapacitors. *Small* 2012, 8, 1805−1834.

(6) Frackowiak, E. Carbon Materials for Supercapacitor Application. *Phys. Chem. Chem. Phys.* 2007, 9, 1774−1785.

(7) Xu, B.; Wu, F.; Chen, R. J.; Cao, G. Q.; Chen, Sh.; Zhou, Zh. M.; Yang, Y. Sh. Highly Mesoporous and High Surface Area Carbon: A High Capacitance Electrode Material for EDLCs with Various Electrolytes. *Electrochem. Commun.* 2008, 10, 795−797.

(8) Futaba, D. N.; Hata, K.; Yamada, T.; Hiraoka, T.; et al. Shape-Engineerable and Highly Densely Packed Single-Walled Carbon Nanotubes and Their Application as Super-Capacitor Electrodes. *Nat. Mater.* 2006, 5, 987−994.

(9) An, K. H.; Kim, W. S.; Park, Y. S.; Moon, J. M.; Bae, D. J.; Lim, S. C.; Lee, Y. S.; Lee, Y. H. Electrochemical Properties of High-Power Supercapacitors Using Single-Walled Carbon Nanotube Electrodes. *Nano Lett.* 2012, 12, 3803−3807.

(10) Zhang, L. L.; Zhou, R.; Zhao, X. S. Graphene-Based Materials as Supercapacitor Electrodes. *J. Mater. Chem.* 2010, 20, 5983−5992.

(11) Choi, B. G.; Yang, M. H.; Hong, W. H.; Choi, J. W.; Huh, Y. S. 3D Macroporous Graphene Frameworks for Supercapacitors with High Energy and Power Densities. *ACS Nano* 2012, 5, 4020−4028.

(12) Chen, J. F.; Lang, Zh. L.; Xu, Q.; Zhang, J. N.; Fu, J. W.; Chen, Zh. M. A Novel Method to Fabricate Discrete Porous Carbon Hemispheres and Their Electrochemical Properties as Supercapacitors. *Phys. Chem. Chem. Phys.* 2013, 15, 17786−17792.

(13) Fu, J. W.; Chen, Zh. M.; Xu, Q.; Chen, J. F.; Huang, X. B.; Tang, X. Zh. The Production of Porous Carbon Nanofibers from Cross-linked Polyphosphazene Nanofibers. *Carbon.* 2011, 49, 1037−1039.

(14) Fu, J. W.; Xu, Q.; Chen, J. F.; Chen, Zh. M.; Huang, X. B.; Tang, X. Zh. Controlled Fabrication of Uniform Hollow Core Porous Shell Carbon Spheres by the Pyrolysis of Core/Shell Polystyrene/Cross-Linked Polyphosphazene Composites. *Chem. Commun.* 2010, 46, 6563−6565.

(15) Li, Y.; Chen, J. F.; Xu, Q.; He, L. H.; Chen, Zh. M. A Controllable Route to Solid and Hollow-Monodisperse-Carbon Nanospheres. *J. Phys. Chem. C* 2009, 113, 10085−10089.

(16) Zhang, X. T.; Chen, L.; Yuan, T. Y.; et al. Dendrimer-Linked, Renewable and Magnetic Carbon Nanotube Aerogels. *Mater. Horiz.* 2014, 1, 232−236.

(17) Huang, H.; Chen, P. W.; Zhang, X. T.; Lu, Y.; Zhan, W. Ch. Edge-to-Edge Assembled Graphene Oxide Aerogels with Outstanding Mechanical Performance and Superhigh Chemical Activity. *Small.* 2013, 8, 1397−1404.

(18) Chen, L.; Wei, B.; Zhang, X. T.; Li, Ch. Bifunctional Graphene/γ-Fe_2O_3 Hybrid Aerogels with Double Nanocrystalline Networks for Enzyme Immobilization. *Small.* 2013, 13, 2331−2340.

(19) Zhong, Sh. L.; Song, J. M.; Zhang, S.; Yao, H. B.; Xu, A. W.; Yao, W. T.; Yu, Sh. H. Template-Free Hydrothermal Synthesis and Formation Mechanism of Hematite Microrings. *J. Phys. Chem. C* 2008, 112, 19916−19921.

(20) Lei, Zh. B.; Zhang, J. T.; Zhao, X. S. Ultrathin MnO_2 Nanofibers Grown on Graphitic Carbon Spheres as High-performance Asymmetric Supercapacitor Electrodes. *J. Mater. Chem.* 2012, 22, 153−160.

(21) Cottineau, T.; Toupin, M.; Delahaye, T.; BroussE, T.; Belanger, D. Nanostructured Transition Metal Oxides for Aqueous Hybrid Electrochemical Supercapacitors. *Appl. Phys. A: Mater. Sci. Process.* **2006**, *82*, 599−606.

(22) Jiang, H.; Ma, J.; Li, Ch. Zh. Mesoporous Carbon Incorporated Metal Oxide Nanomaterials as Supercapacitor Electrodes. *Adv. Mater.* **2012**, *24*, 4197−4202.

(23) Lang, X. Y.; Hirata, A.; Fujita, T.; Chen, M. W. Nanoporous Metal/Oxide Hybrid Electrodes for Electrochemical Supercapacitors. *Nat. Nanotechnol.* **2011**, *6*, 232−236.

(24) Hu, L. B.; Choia, J. W.; Yang, Y.; Jeong, S.; Mantia, F. L.; Cui, L. F.; Cui, Y. Highly Conductive Paper for Energy-Storage Devices. *Proc. Nat'l. Acad. Sci.* **2009**, *106*, 21490−21494.

(25) Zhao, G. Y.; Li, H. L. Preparation of Polyaniline Nanowire Arrayed Electrodes for Electrochemical Supercapacitors. *Microporous Mesoporous Mater.* **2008**, *110*, 590−594.

(26) Fan, L. Zh.; Maier, J. High-Performance Polypyrrole Electrode Materials for Redox Supercapacitors. *Electrochem. Commun.* **2006**, *8*, 937−940.

(27) Alvi, F.; Ram, M. K.; Basnayaka, P.; Stefanakos, E.; Goswami, Y.; Hoff, A. M.; Kumar, A. Electrochemical Supercapacitors Based on Graphene-Conducting Polythiophenes Nanocomposite. *ECS Trans.* **2011**, *35*, 167−174.

(28) Yu, G. H.; Hu, L. B.; Vosgueritchian, M.; Wang, H. L.; et al. Solution-Processed Graphene/MnO₂ Nanostructured Textiles for High-Performance Electrochemical Capacitors. *Nano Lett.* **2011**, *11*, 2905−2911.

(29) Li, Q.; Wang, Z. L.; Li, G. R.; Guo, R.; Ding, L. X.; Tong, Y. X. Design and Synthesis of MnO₂/Mn/MnO₂ Sandwich-Structured Nanotube Arrays with High Supercapacitive Performance for Electrochemical Energy Storage. *Nano Lett.* **2012**, *12*, 3803−3807.

(30) Yu, G. H.; Hu, L. B.; Liu, N.; Wang, H. L.; Vosgueritchian, M.; Yang, Y.; Cui, Y.; Bao, Zh. N. Enhancing the Supercapacitor Performance of Graphene/MnO₂ Nanostructured Electrodes by Conductive Wrapping. *Nano Lett.* **2011**, *11*, 4438−4442.

(31) Yan, J.; Fan, Zh. J.; Wei, T.; Qian, W. Zh.; Zhang, M. L.; Wei, F. Fast and Reversible Surface Redox Reaction of Graphene-MnO₂ Composites as Supercapacitor Electrodes. *Carbon.* **2010**, *48*, 3825−3833.

(32) Zhi, M. J.; Xiang, Ch.; Li, J. T.; Li, M.; Wu, N. Q. Nanostructured Carbon-Metal Oxide Composite Electrodes for Supercapacitors: A Review. *Nanoscale.* **2013**, *5*, 72−88.

(33) Grzyba, B.; Hildenbranda, C.; Berthon-Fabrya, S.; Beginb, D.; Jobc, N.; Rigaccia, A.; Acharda, P. Functionalisation and Chemical Characterization of Cellulose-Derived Carbon Aerogels. *Carbon.* **2010**, *48*, 2297−2307.

(34) Jin, Y.; Chen, H. Y.; Chen, M. H.; Liu, N.; Li, Q. W. Graphene-Patched CNT−MnO₂ Nanocomposite Papers for the Electrode of High-Performance Flexible Asymmetric Supercapacitors. *ACS Appl. Mater. Interfaces* **2013**, *5*, 3408−3416.

(35) Hu, B.; Yu, Sh. H.; Wang, K.; Liu, L.; Xu, X. W. Functional Carbonaceous Materials from Hydrothermal Carbonization of Biomass: An Effective Chemical Process. *Dalton Trans.* **2008**, 5414−5423.

(36) Titirici, M. M.; White, R. J.; Falcoa, C.; Sevilla, M. Black Perspectives for a Green Future: Hydrothermal Carbons for Environment Protection and Energy Storage. *Energy Environ. Sci.* **2012**, *5*, 6796−6822.

(37) White, R. J.; Budarin, V.; Luque, R.; Clark, J. H.; Macquarrie, D. Tuneable Porous Carbonaceous Materials from Renewable Resources. *Chem. Soc. Rev.* **2009**, *38*, 3401−3418.

(38) Falco, C.; Baccile, N.; Titirici, M. M. Morphological and Structural Differences between Glucose, Cellulose and Lignocellulosic Biomass Derived Hydrothermal Carbons. *Green Chem.* **2011**, *13*, 3273−3281.

(39) Titirici, M. M.; Antonietti, M. Chemistry and Materials Options of Sustainable Carbon Materials Made by Hydrothermal Carbonization. *Chem. Soc. Rev.* **2010**, *39*, 103−116.

(40) Xu, Y. X.; Sheng, K. X.; Li, Ch.; Shi, G. Q. Self-Assembled Graphene Hydrogel via a One-Step Hydrothermal Process. *ACS Nano* **2010**, *4*, 4324−4330.

(41) Brun, N.; Gonzalez, C. A. G.; Smirnova, I.; Titirici, M. M. Hydrothermal Synthesis of Highly Porous Carbon Monoliths from Carbohydrates and Phloroglucinol. *RSC Adv.* **2013**, *3*, 17088−17096.

(42) Wu, X. L.; Wen, T.; Guo, H. L.; Yang, Sh. B.; Wang, X. K.; Xu, A. W. Biomass-Derived Sponge-like Carbonaceous Hydrogels and Aerogels for Supercapacitors. *ACS Nano* **2013**, *4*, 3589−3597.

(43) Krishnan, D.; Raidongia, K.; Shao, J. J.; Huang, J. X. Graphene Oxide Assisted Hydrothermal Carbonization of Carbon Hydrates. *ACS Nano* **2014**, *8*, 449−457.

(44) Xue, Zh. X.; Wang, Sh. T.; Lin, L.; Chen, L.; Liu, M. J.; Feng, L.; Jiang, L. A Novel Superhydrophilic and Underwater Superoleophobic Hydrogel-Coated Mesh for Oil/Water Separation. *Adv. Mater.* **2011**, *23*, 4270−4273.

(45) Chen, Sh.; Zhu, J. W.; Wu, X. D.; Han, Q. F.; Wang, X. Graphene Oxide−MnO₂ Nanocomposites for Supercapacitors. *ACS Nano* **2010**, *4*, 2822−2830.

(46) Lee, S. W.; Bak, S. M.; Lee, Ch. W.; et al. Structural Changes in Reduced Graphene Oxide upon MnO₂ Deposition by the Redox Reaction between Carbon and Permanganate Ions. *J. Phys. Chem. C* **2014**, *118*, 2834−2843.

(47) Chen, W.; Rakhi, R. B.; Hu, L. B.; Xie, X.; Cui, Y.; Alshareef, H. N. High-Performance Nanostructured Supercapacitors on a Sponge. *Nano Lett.* **2011**, *11*, 5165−5172.

(48) Wang, F.; Dai, H. X.; Deng, J. G.; Bai, G. M.; Ji, K. M.; Liu, Y. X. Manganese Oxides with Rod-, Wire-, Tube-, and Flower-Like Morphologies: Highly Effective Catalysts for the Removal of Toluene. *Environ. Sci. Technol.* **2012**, *46*, 4034−4041.

(49) Chen, W. M.; Qie, L.; Shao, Q. G.; Yuan, L. X.; Zhang, W. X.; Huang, Y. H. Controllable Synthesis of Hollow Bipyramid β-MnO₂ and Its High Electrochemical Performance for Lithium Storage. *ACS Appl. Mater. Interfaces* **2012**, *4*, 3047−3053.

(50) Wang, X.; Li, Y. D. Selected-Control Hydrothermal Synthesis of α- and β-MnO₂ Single Crystal Nanowires. *J. Am. Chem. Soc.* **2012**, *12*, 2880−2881.

(51) Li, Zh. Q.; Ding, Y.; Xiong, Y. J.; Yang, Q.; Xie, Y. One-Step Solution-Based Catalytic Route to Fabricate Novel α-MnO₂ Hierarchical Structures on a Large Scale. *Chem. Commun.* **2005**, 918−920.

(52) Sharma, R. K.; Oh, H. S.; Shul, Y. G.; Kim, H. Carbon-Supported, Nano-structured, Manganese Oxide Composite Electrode for Electrochemical Supercapacitor. *J. Power Sources* **2007**, *173*, 1024−1028.

(53) Tadjer, M. J.; Mastro, M. A.; Rojo, J. M.; et al. MnO₂-Based Electrochemical Supercapacitors on Flexible Carbon Substrates. *J. Electron. Mater.* **2014**, *43*, 1188−1193.

(54) Peng, Y. T.; Chen, Zh.; Wen, J.; et al. Hierarchical Manganese Oxide/Carbon Nanocomposites for Supercapacitor Electrodes. *Nano Res.* **2011**, *4*, 216−225.

(55) Zhao, G. X.; Li, J. X.; Jiang, L.; Dong, H. L.; Wang, X. K.; Hu, W. P. Synthesizing MnO₂ Nanosheets from Graphene Oxide Templates for High Performance Pseudosupercapacitors. *Chem. Sci.* **2012**, *3*, 433−437.

(56) Zolfaghari, A.; Naderi, H. R.; Mortaheb, H. R. Carbon Black/Manganese Dioxide Composites Synthesized by Sonochemistry Method for Electrochemical Supercapacitors. *J. Electroanal. Chem.* **2013**, *697*, 60−67.

(57) Sharma, R. K.; Oh, H. S.; Shul, Y. G.; Kim, H. Growth and Characterization of Carbon-Supported MnO₂ Nanorods for Supercapacitor Electrode. *Physica B* **2008**, *403*, 1763−1769.

(58) Liang, Y. R.; Liang, F. X.; Zhong, H.; Li, Zh. H.; Fu, R. W.; Wu, D. C. An Advanced Carbonaceous Porous Network for High-Performance Organic Electrolyte Supercapacitors. *J. Mater. Chem. A* **2013**, *1*, 7000−7005.

(59) Yu, G. H.; Hu, L. B.; Liu, N.; et al. Enhancing the Supercapacitor Performance of Graphene/MnO₂ Nanostructured Electrodes by Conductive Wrapping. *Nano Lett.* **2011**, *11*, 4438−4442.

(60) Chen, Ch. Y.; Fan, C. Y.; Lee, M. T.; Chang, J. K. Tightly Connected MnO_2−Graphene with Tunable Energy Density and Power Density for Supercapacitor Application. *J. Mater. Chem.* **2012**, *22*, 7697−7700.

(61) Xiao, F.; Li, Y. Q.; Zan, X. L.; Liao, K.; Xu, R.; Duan, H. W. Growth of Metal−Metal Oxide Nanostructures on Freestanding Graphene Paper for Flexible Biosensors. *Adv. Funct. Mater.* **2012**, *22*, 2487−2494.

(62) Li, Zh. P.; Mi, Y. J.; Liu, X. H.; Liu, Sh.; Yang, Sh. R.; Wang, J. Q. Flexible Graphene/MnO_2 Composite Papers for Supercapacitor Electrodes. *J. Mater. Chem.* **2011**, *21*, 14706−14711.

(63) Wang, J. G.; Yang, Y.; Huang, Zh. H.; Kang, F. Y. A High-Performance Asymmetric Supercapacitor Based on Carbon and Carbon−MnO_2 Nanofiber Electrodes. *Carbon* **2013**, *61*, 190−199.